Frequency-Adaptive Current Controller for Three-Phase Grid-Connected Converters

Sebastián Gómez Jorge, Claudio A. Busada, and Jorge A. Solsona, *Senior Member, IEEE*

***Abstract*—This paper analyzes the behavior of a nonfrequency-adaptive reduced-order-generalized-integrator-based current controller when the grid frequency is subject to variations and proposes a simple method for making it frequency adaptive. The proposed frequency adaptation scheme allows to keep the good performance of the current controller even in the presence of frequency variations. The resulting frequency-adaptive controller has very low computational burden, and it is therefore suitable for low-cost digital-signal-processor implementation.**

***Index Terms*—Current controller, frequency adaptive, reduced order generalized integrator (ROGI), voltage source converter (VSC).**

I. Introduction

POWER GENERATION through the use of distributed power generation system (DPGS) has grown in the last few years [1]. Aside from being used to provide energy to isolated grids, there is also an increasing trend toward the usage of DPGS in supplying power to the mains grid [2], [3]. In these applications, both a robust current control algorithm and a grid synchronization strategy are usually required. There are numerous current control techniques, some of which are reviewed in [4]. Among these, we can find deadbeat controllers [5], [6], hysteresis controllers [7]–[9], and current controllers based on resonant filters [10], [11]. Most of these schemes must be used in conjunction with a synchronization algorithm capable of recovering the phase of the fundamental component of the grid voltage. Some, like the resonant controllers, might also require knowledge of its frequency in order to adjust their own resonance frequency in the presence of grid frequency variations. This is done to avoid a performance decrease during these variations. Among the typical synchronization algorithms, there are those based on the use of phase-locked loops [12], [13], second-order generalized integrators or adaptive notch filters [14], [15], and sequence sensitive resonant filters [16], [17]. The combination of both the current control strategy and the synchronization algorithm can usually result in high implementation costs, either from the viewpoint of memory requirements or computational burden.

In [18], a three-phase nonfrequency-adaptive current controller based on reduced order generalized integrators (ROGIs) was proposed. The ROGIs are sensitive to both frequency and sequence, which allows, in low imbalance grids, to reduce the computational burden of the controller. Another interesting feature of this scheme is that it does not require knowledge of the fundamental component of the grid voltage in order to produce balanced high quality injected currents.

This paper will analyze the impact of the grid voltage frequency variations on the performance of the ROGI-based controller. It will be shown that a grid frequency offset around its nominal value decreases the quality of the injected currents because the controller can no longer exactly compensate the distorting effects of the grid voltage harmonics. One way to deal with this would be to implement one of the aforementioned grid synchronization techniques to estimate the grid frequency and use it to tune the resonance frequency of the ROGIs. This would undoubtedly increase the computational burden of the implementation due to the addition of the synchronization algorithm. This paper proposes another way: By taking advantage of the ROGI-based controller structure, a very simple and low computational burden frequency estimation algorithm can be performed. The main features of this proposal are as follows.

1) It allows to keep the ROGIs of the current controller tuned, even if there is a mismatch between the actual grid frequency and its nominal value. This prevents the currents from being distorted in the presence of frequency variations.
2) The frequency estimator requires only one additional state to be built and a small number of operations to compute the frequency, which makes it ideal for a low-cost digital signal processor (DSP) implementation.

The proposed estimation algorithm merges seamlessly with the ROGI-based controller and, as will be shown, increases its performance noticeably. This paper is organized as follows. First, in Section II, a description of the controller/plant system is given. Then, in Section III, the working principles behind the ROGI-based current controller are discussed. Section IV shows the effects of frequency variation on the controller's performance. Section V describes the proposed frequency estimation algorithm and gives a method for choosing its design parameters. Sections VI and VII show simulation and experimental results, respectively, which validate the proposal. Finally, in Section VIII, conclusions are drawn.

Manuscript received March 6, 2012; revised June 5, 2012; accepted July 7, 2012. Date of publication July 19, 2012; date of current version May 16, 2013. This work was supported in part by Universidad Nacional del Sur, by Consejo Nacional de Investigaciones Científicas y Técnicas, and by Agencia Nacional de Promoción Científica y Tecnológica, Argentina.

The authors are with Instituto de Investigaciones en Ingeniería Eléctrica "Alfredo Desages" (Universidad Nacional del Sur (UNS)–CONICET), Departamento de Ingeniería Eléctrica y de Computadoras, UNS, 8000 Bahía Blanca, Argentina (e-mail: sebastian.gomezjorge@uns.edu.ar; cbusada@uns.edu.ar; jsolsona@uns.edu.ar).

Digital Object Identifier 10.1109/TIE.2012.2209617

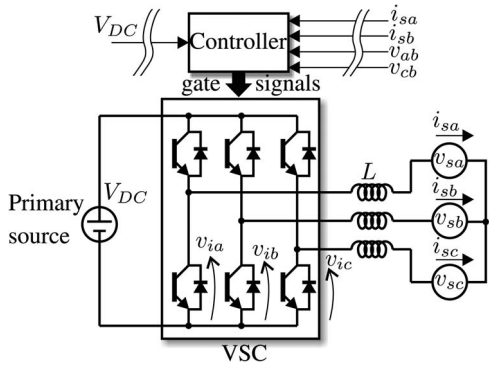

Fig. 1. DPGS description.

II. System Description

Fig. 1 shows the physical description of a standard three-phase DPGS. It consists of a three-phase voltage source converter (VSC), whose output voltages are v_{ia}, v_{ib}, v_{ic}, and three L valued inductances, which are the coupling elements between the converter and the grid. The primary source delivers a dc voltage V_{DC} to the VSC bus. The three-phase grid is represented by its respective phase voltages, v_{sa}, v_{sb}, and v_{sc}. The control of the VSC is performed by a DSP, which is represented by the block "Controller." This DSP samples the measurement of two phase currents, two line voltages, and the bus voltage, and after processing these, it generates the gate signals which trigger the switches of the VSC.

Due to the discrete nature of the controller, the whole system is modeled in this paper in the discrete time domain, as shown in Fig. 2. This figure has two blocks, "Plant" and "Current controller." The block "Plant" encompasses the discrete time model of the coupling inductors, as well as a discrete time model of the DSP processing delay. The coupling inductance behavior is modeled through the zero order hold discretization of their differential equations, which yields the discrete Euler forward integrator shown in the figure [19]. In Fig. 2, the variables are described in the stationary reference frame [20], denoted by the superscript $\alpha\beta$, using complex space vector representation [21]. The perturbation effect of the grid voltage on the plant is modeled through the grid average voltage $\vec{v}_s^{\alpha\beta}$, the grid current is referred to as $\vec{i}^{\alpha\beta}$, the VSC output voltage is $\vec{v}_i^{\alpha\beta}$, and the output of the current controller is the control signal $\vec{u}_c^{\alpha\beta}$. Since the control signal is reproduced by the VSC after the DSP processing delay (signal $\vec{v}_i^{\alpha\beta}$), for convenience, this delay has been included as part of the plant model. It can be a fraction $\tau \leq T_s$ of the sampling time T_s and is modeled here through the transfer function

$$D(z) = d_1 + d_2 z^{-1} \tag{1}$$

where $d_1 = 1 - \tau/T_s$ and $d_2 = \tau/T_s$, and z is the $\mathcal{Z}$-transform variable [18]. The nonlinearities of the VSC (dead times and voltage drops) are neglected; hence, the converter is considered as a unitary gain. The control signal $\vec{u}_c^{\alpha\beta}$ is generated by the block "Current controller," which is explained in detail in the following section.

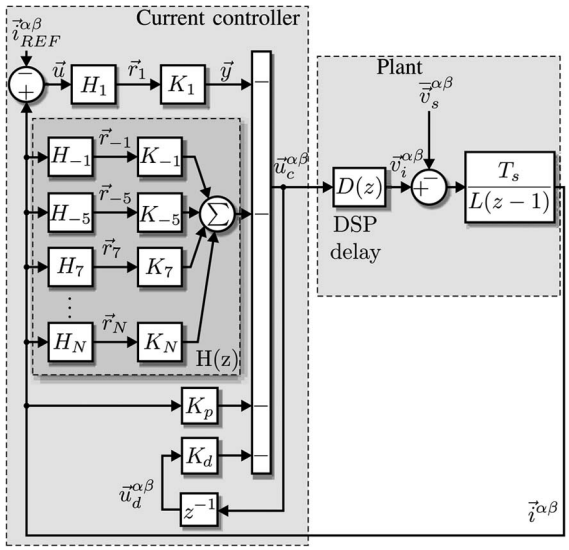

Fig. 2. Plant and current controller discrete time model.

III. Nonfrequency-Adaptive ROGI-Based Current Controller

The objective of most DPGSs is to inject balanced sinusoidal currents of fundamental frequency to the grid. These currents must have a very low total harmonic distortion (THD). Since the grid voltage represents a disturbance in the system, the controller is required to have the ability to both track the fundamental positive sequence component of the grid voltage and also reject the harmonic components present in this voltage. A ROGI-based controller can attain these goals with a very low computational burden [18]. The low burden is a result of the use of ROGIs, which allow to compensate specific frequency and sequence harmonics, avoiding unnecessary computations. Additionally, this controller avoids the need to obtain the fundamental positive sequence component of the grid voltage for synchronization. In the following, the working principles of the ROGI-based controller will be presented.

The ROGI-based controller is shown in the block "Current controller" of Fig. 2. The building block of this controller is the ROGI, whose transfer function is

$$H_h(z) = \frac{1}{z - e^{hj\hat{\omega}T_s}} \tag{2}$$

where $h \in \mathbb{Z}$, $j = \sqrt{-1}$, and $\hat{\omega}$ is the fundamental resonance angular frequency. The Bode plot of the fundamental ROGI H_1 present in Fig. 2 is shown in Fig. 3, evaluating $H_1(e^{jT_s\Omega})$. In this Bode, positive frequencies denote response to a positive sequence input signal vector, whereas negative frequencies denote response to a negative sequence one. As can be seen, this ROGI provides infinite gain to a positive sequence fundamental frequency signal. Through proper selection of h in (2), the ROGI can be tuned to provide infinite gain to specific frequencies and sequences of interest.

In the controller shown in Fig. 2, ROGIs are placed in a feedback loop between the current $\vec{i}^{\alpha\beta}$ and the control action $\vec{u}_c^{\alpha\beta}$. These ROGIs are the fundamental ROGI $H_1(z)$ and the

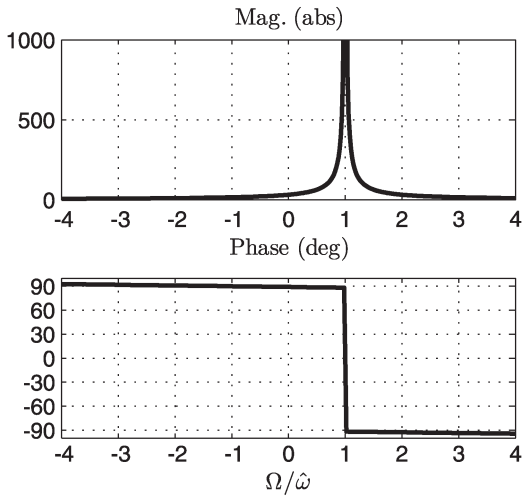

Fig. 3. ROGI $H_1(e^{jT_s\Omega})$ Bode plot.

harmonic compensation ROGIs found inside $H(z)$, which is defined as

$$H(z) = \sum_{\substack{h \\ h\neq 1}} K_h H_h(z) \tag{3}$$

where $K_h \in \mathbb{C}$ is a design constant. The fundamental ROGI is placed at the output of the error signal $\vec{u} = \vec{i}^{\alpha\beta}_{\text{REF}} - \vec{i}^{\alpha\beta}$ and is used to force the current $\vec{i}^{\alpha\beta}$ to track the positive sequence fundamental component of the reference current $\vec{i}^{\alpha\beta}_{\text{REF}}$ (since $H_1(z)$ has infinite gain to that frequency and sequence). The harmonic compensation block $H(z)$ is used to force any harmonic perturbation present in $\vec{i}^{\alpha\beta}$ to zero. Note that, for this to actually happen, $H(z)$ must have a ROGI for each harmonic component present in $\bar{\vec{v}}^{\alpha\beta}_s$ because this voltage represents a perturbation to the plant. Hence, if, for example, the grid voltage had the 7th and 13th positive sequence harmonics and the 1st, 5th, and 11th negative sequence harmonics, then $H(z) = H_7(z) + H_{13}(z) + H_{-1}(z) + H_{-5} + H_{-11}(z)$ would be required to compensate them all.

Since, in most DPGSs, the objective is to inject balanced currents in phase with the fundamental component of the grid voltage, the reference current is chosen to be

$$\vec{i}^{\alpha\beta}_{\text{REF}} = g\vec{v}^{\alpha\beta}_s \tag{4}$$

where $g \in \mathbb{R}$, $g > 0$ is a constant that determines the magnitude of the injected current, and $\vec{v}^{\alpha\beta}_s$ is the measured instantaneous grid voltage. Note that this reference current will have the same harmonic content as the grid voltage. However, if all the grid harmonics are modeled in $H(z)$, the reference current harmonics will also be compensated.

Regarding the constant g, it will usually come from an external control loop. For example, in a photovoltaic application, a maximum power point tracking algorithm can be used to vary the dc bus voltage reference point, and using a simple proportional-integral controller, a value of g that will make the actual dc bus voltage move toward this reference value can be obtained. These applications escape the scope of this paper, so g will be considered a given constant reference value.

The controller gains K_h, K_p, and K_d provide a full state feedback (in fact, note in Fig. 2 that K_d feeds back a signal equal to the internal state of the block "DSP delay"). In this paper, the gains are chosen via the linear quadratic regulator (LQR) method, assuming $\hat{\omega} = \omega_o$, where ω_o is the nominal grid frequency. The guidelines used here for choosing the weighting factors of the LQR are described in Appendix I. The feedback gains K_h, K_p, and K_d obtained via the LQR method have no impact on either the steady-state harmonic rejection capabilities or the steady-state fundamental component tracking capabilities of the ROGI-based current controller. However, these gains change the pole locations of the closed-loop transfer functions and therefore determine the transient response of the closed-loop system [18].

Under nominal frequency conditions, the ROGI-based current controller works well. However, its main drawback is that, without a frequency estimation algorithm that updates the fundamental resonance frequency in (2) to the grid frequency, the THD of the injected currents degrades in the presence of frequency variations, and for imbalanced systems, the injected current is no longer balanced. This is shown in the following section.

IV. Effects of Frequency Variations on the Controller's Performance

We will now analyze the effects of frequency variations on the injected currents when using a ROGI-based controller without frequency adaptation. These effects are as follows:

1) an increase in the current THD;
2) current imbalance;
3) phase error between the injected current and the fundamental positive sequence component of the grid voltage.

To quantify these, we will analyze the steady-state behavior of the system by means of its frequency response. The open-loop state variable description of the system shown in Fig. 2 results

$$\vec{x}(k+1) = A\vec{x}(k) + B\vec{u}^{\alpha\beta}_c(k) + B_v\bar{\vec{v}}^{\alpha\beta}_s(k) \tag{5}$$

where

$$\underbrace{\begin{bmatrix} 1 & \frac{d_2T_s}{L} & 0 & \dots & 0 \\ 0 & 0 & 0 & \dots & 0 \\ 1 & 0 & e^{j\hat{\omega}T_s} & \dots & 0 \\ \vdots & \vdots & \vdots & \ddots & 0 \\ 1 & 0 & 0 & 0 & e^{jN\hat{\omega}T_s} \end{bmatrix}}_{A}; \quad \underbrace{\begin{bmatrix} \frac{d_1T_s}{L} \\ 1 \\ 0 \\ \vdots \\ 0 \end{bmatrix}}_{B}; \quad \underbrace{\begin{bmatrix} -\frac{T_s}{L} \\ 0 \\ -g \\ \vdots \\ 0 \end{bmatrix}}_{B_v} \tag{6}$$

with $\hat{\omega} = \omega_o$ (for the case without frequency adaptation) and the state vector $\vec{x} = [\vec{i}^{\alpha\beta}\ \vec{u}^{\alpha\beta}_d\ \vec{r}_1\ \vec{r}_{-1}\ \dots\ \vec{r}_N]^T$, where $N \in \mathbb{Z}$ is the harmonic order of the last ROGI. The third row of B_v comes from approximating (4) by $\vec{i}^{\alpha\beta}_{\text{REF}}(k) \simeq g\bar{\vec{v}}^{\alpha\beta}_s(k)$, which introduces a negligible error in the Bode analysis. The

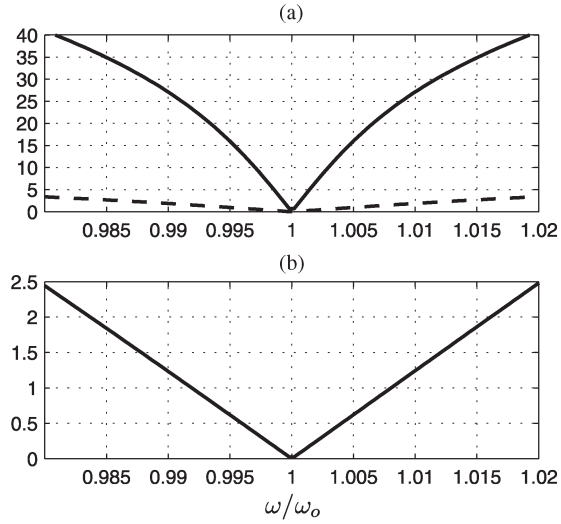

Fig. 4. Frequency variation effects. (a) THD% for (solid) case 1 and (dashed) case 2. (b) Injected current negative sequence % for a pure sinusoidal grid voltage contaminated with a 20% negative sequence component.

frequency response of the closed-loop system can be found by computing

$$G(\Omega) = \left.\frac{\vec{i}^{\alpha\beta}(z)}{\vec{v}_s^{\alpha\beta}(z)}\right|_{e^{jT_s\Omega}} = C(e^{jT_s\Omega}I - A_{\rm cl})^{-1}B_v \qquad (7)$$

where $A_{\rm cl} = A - B_v[K_1 \quad K_{-1} \quad K_{-5} \quad \dots \quad K_N]$, $C = [1\,0\,0\,\dots\,0]$, and I is an identity matrix with $A_{\rm cl}$ dimensions.

The current THD can be found from (7) by means of

$$\text{THD}\% = 100\frac{\sqrt{\sum_{h\neq 1}|G(h\omega)|^2\,V_h^2}}{|G(\omega)|\,V_1} \qquad (8)$$

where V_h is the magnitude of the hth harmonic and ω is the steady-state frequency of the fundamental positive sequence component of the grid voltage.

To show the impact on the current THD, two cases will be analyzed, one assuming a grid voltage in normal operating conditions and another assuming a highly distorted grid voltage. Table I (see Appendix II) shows the magnitude of the harmonic components of the test voltages as a percentage of the 100-Vrms fundamental component for case 1, a highly distorted grid voltage with THD $= 51.5\%$, and case 2, a grid voltage in normal operating conditions with THD $= 5\%$. In both cases, the controller setup was the one shown in Table II (see Appendix II). Fig. 4(a) shows the plots of (8) for cases 1 and 2 when the fundamental frequency ω is allowed a variation of $|\omega - \omega_o| \leq 0.02\omega_o$ around the nominal frequency. As the figure shows, the performance drop is quite significant. Although, for case 2, the THD does not increase as much as for case 1, a 1% frequency variation degrades the THD to almost 2%.

Regarding current imbalance, the frequency mistuning reduces the controller's imbalance rejection capabilities provided by the ROGI $H_{-1}(z)$. This results in an unbalanced current generation, as shown in Fig. 4(b). This figure shows the percentage of current imbalance as the fundamental frequency varies for a pure sinusoidal grid voltage contaminated with a 20% negative sequence component and is obtained evaluating $100\%|G(-\omega)|V_{-1}/V_1$ for $|\omega - \omega_o| \leq 0.02\omega_o$. As can be seen, a 1% frequency variation results in a 1.2% current imbalance.

Regarding the phase error, the frequency variation produces phase errors between the current $\vec{i}^{\alpha\beta}$ and the fundamental component of the grid voltage. These errors can be obtained evaluating $G(\omega)$ for $|\omega - \omega_o| \leq 0.02\omega_o$, although they are usually not significant (4.5° error for a 1% frequency deviation). Although these phase errors can be neglected in most applications, the THD degradation and reduced imbalance rejection capabilities are significant.

In the following section, a frequency estimation algorithm will be developed. This algorithm will allow the controller to avoid the performance drop in the presence of frequency variations.

V. Frequency Estimation

As shown in the previous section, the grid frequency is subject to fluctuations that, although small, affect the performance of the controller. In this section, a fundamental frequency estimation algorithm will be proposed. This estimator only requires one additional state to be performed. The estimated grid frequency $\hat{\omega}$ will be used to update online the resonance frequency of the ROGIs that compose the controller [update of matrix A in (6)]. Since it is not possible to recalculate the controller gains K_h, K_p, and K_d online for each value of $\hat{\omega}$, which would require a large computation effort in a low-cost DSP implementation, we will use as fixed gains those obtained for $\hat{\omega} = \omega_o$, even when $\hat{\omega}$ is updated with a frequency estimator. It is therefore necessary to analyze the stability of the closed-loop system when the estimated frequency $\hat{\omega} \neq \omega_o$ varies within the expected grid frequency variation range in normal operating conditions.

A. Closed-Loop Stability for $\hat{\omega} \neq \omega_o$

It is to be expected that the closed-loop system's dynamics will not change significantly when $\hat{\omega}$ varies in (6) within the normal grid frequency variation range since this frequency is only allowed small deviations from its nominal value. However, this must always be checked, since the LQR method, although in general produces robust controllers, does not guarantee stability for arbitrary variations of $\hat{\omega}$. Assuming a $\pm 2\%$ frequency variation, the closed-loop stability can be easily checked by computing the modulus of the eigenvalues of matrix $A_{\rm cl}$, defined in (7), and then verifying that the maximum modulus is always smaller than unity as $\hat{\omega}$ varies. For the system described in Table II, such a plot is shown in Fig. 5. The fact that the maximum modulus eigenvalue of $A_{\rm cl}$ is less than unity for the expected frequency variation range ensures that the closed-loop system will remain stable as $\hat{\omega}$ is updated.

Having checked the system stability, we will now proceed to develop a frequency estimation algorithm.

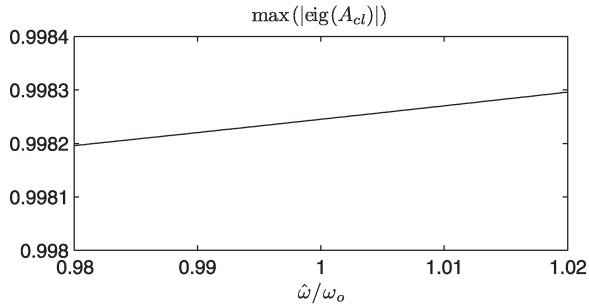

Fig. 5. Maximum closed-loop eigenvalue module for $0.98\omega_o \leq \hat{\omega} \leq 1.02\omega_o$.

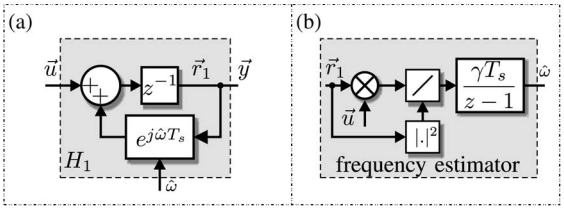

Fig. 6. Frequency estimation. (a) Fundamental ROGI block diagram. (b) Frequency estimator.

B. Frequency Estimation Algorithm

The idea of the proposed frequency estimator is to take advantage of the controller structure to recover the fundamental frequency with a small number of operations. Let us look again at the Bode plot of the fundamental ROGI shown in Fig. 3, considering $\vec{u}$ as its input and $\vec{r}_1$ as its output, as shown in Fig. 6(a). If $\vec{u}$ is a positive sequence sinusoidal signal of frequency ω and the ROGI is tuned at a frequency $\hat{\omega} > \omega$, then the steady-state magnitude and phase of the ROGI output will be somewhere to the left of $\Omega/\hat{\omega} = 1$ in Fig. 3. Note that, for any $\hat{\omega} > \omega$, the output leads the input by almost 90°. Similarly, if $\hat{\omega} < \omega$, then the steady-state magnitude and phase of the ROGI output will be somewhere to the right of $\Omega/\hat{\omega} = 1$. Hence, $\vec{r}_1$ will lag $\vec{u}$ by almost 90°. Therefore, the sign of the phase difference between $\vec{r}_1$ and $\vec{u}$ can be used to determine whether the estimated frequency $\hat{\omega}$ should be increased or decreased. The sign of the phase difference can be obtained by computing the cross product between $\vec{u}$ and $\vec{r}_1$ since $\vec{r}_1(k) \otimes \vec{u}(k) = |\vec{r}_1(k)||\vec{u}(k)| \sin\phi$, where $\phi = \angle\vec{u} - \angle\vec{r}_1$ [16]. Additionally, if the ROGI is tuned exactly at the input frequency ($\hat{\omega} = \omega_o$ for a nominal frequency input signal), it will present an infinite gain to that frequency. In this situation, the closed-loop system will force $\vec{u}$ to zero (assuming that the grid is a pure sinusoidal positive sequence signal). As a result, the cross product will yield zero, which shows that an equilibrium is reached once the estimated frequency converges to the actual frequency. If the grid had harmonics, this reasoning would still hold, but instead of reaching an equilibrium point, the cross product would have a ripple whose magnitude would depend on the aforementioned harmonic content.

Since the cross product only indicates the direction in which $\hat{\omega}$ should be moved (increased, decreased, or left unchanged), then the estimated frequency update algorithm is implemented as the actual estimated frequency plus a scaled version of this cross product, resulting in

$$\hat{\omega}(k+1) = \text{sat}\left(\gamma T_s \frac{\vec{r}_1(k) \otimes \vec{u}(k)}{|\vec{r}_1(k)|^2} + \hat{\omega}(k)\right) \tag{9}$$

where $\gamma \in \mathbb{R}$, $\gamma > 0$ is a design constant that determines the convergence speed of the estimator, and sat() is a saturation, which clamps the estimated frequency between the minimum and maximum expected frequencies for a grid operating in normal conditions (in this case, $\pm 2\%\omega_o$). The normalization in (9) is performed so that $\hat{\omega}$ converges in mean value to the actual grid frequency, which will be shown in the following section. This estimator is illustrated in the block diagram representation shown in Fig. 6(b). The implementation of (9) requires only two add, three product, and one division operations.

C. Steady-State Analysis and Parameter Tuning

We will now show, assuming a pure sinusoidal grid, that, in steady state, the proposed estimator converges to the fundamental frequency ω. From Fig. 6(a), $\vec{r}_1$ can be written as

$$\vec{r}_1(k+1) = \vec{u}(k) + e^{j\hat{\omega}T_s}\vec{r}_1(k). \tag{10}$$

Performing the cross product with $\vec{r}_1(k)$ on both sides of this equation and then operating, it can be found that the cross product in (9) results

$$\frac{\vec{r}_1 \otimes \vec{u}}{|\vec{r}_1|^2} = \frac{\vec{r}_1(k) \otimes \vec{r}_1(k+1) - \vec{r}_1(k) \otimes e^{j\hat{\omega}T_s}\vec{r}_1(k)}{|\vec{r}_1(k)|^2}. \tag{11}$$

If the sampling period T_s is small enough with respect to the convergence speed of $\vec{r}_1$ so that $|\vec{r}_1(k+1)| \simeq |\vec{r}_1(k)|$ and $\omega_r(k+1) \simeq \omega_r(k)$, where ω_r is the instantaneous frequency of $\vec{r}_1$, then (11) becomes

$$\frac{\vec{r}_1 \otimes \vec{u}}{|\vec{r}_1|^2} \simeq \sin(\omega_r T_s) - \sin(\hat{\omega}T_s) \simeq T_s(\omega_r - \hat{\omega}) \tag{12}$$

where the last approximation is valid if T_s is small enough so that $\sin(\omega_r T_s) \simeq \omega_r T_s$ and $\sin(\hat{\omega}T_s) \simeq \hat{\omega}T_s$. Assuming that (12) holds, the estimated frequency (9) results

$$\hat{\omega} = \frac{\gamma T_s^2}{z - 1 + \gamma T_s^2}\omega_r \tag{13}$$

which shows that $\hat{\omega}$ and ω_r are related through a first-order low-pass filter with a pole in $z = 1 - \gamma T_s^2$. Therefore, it is concluded that, in steady state, $\hat{\omega}$ converges to ω_r. Since the controller is closed loop stable, as shown in Section V-A, and it is a linear system, in steady state, ω_r must necessarily converge to the fundamental grid frequency ω. Then, (13) implies that $\hat{\omega}$ converges to ω. This provided that the convergence speed of (9) is slow enough so that $\hat{\omega}$ can be considered slow varying with respect to ω_r, ensuring the convergence of (13) and the closed-loop stability of the frequency estimator. Also, if the grid had harmonic content, it is to be expected that the ripple in the frequency estimation produced by these harmonics is reduced since (13) represents a low-pass filter.

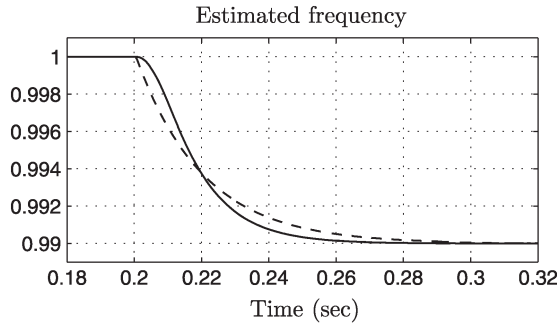

Fig. 7. Frequency estimator dynamic response. (Solid) Actual estimated frequency and (dashed) approximation through (14).

Neglecting the dynamic between ω_r and ω by replacing ω_r with ω in (13), we obtain

$$\hat{\omega} \simeq \frac{\gamma T_s^2}{z - 1 + \gamma T_s^2}\omega. \tag{14}$$

This equation can be used to choose γ to achieve the desired setting time to 2% of the final value of ω without significant error. For the first-order discrete transfer function shown in (14), this setting time is given by

$$t_{\text{set}} \simeq \frac{4T_s}{\sigma} \tag{15}$$

where $\sigma = -\ln(1 - \gamma T_s^2)$ [19]. Therefore

$$\gamma = \frac{1 - e^{-\frac{4T_s}{t_{\text{set}}}}}{T_s^2}. \tag{16}$$

Choosing $t_{\text{set}} = 80$ ms gives a good tradeoff between convergence speed and harmonic filtering capabilities and results in $\gamma \simeq 5 \times 10^5$ for $T_s = 100$ μs. Using this γ, Fig. 7 shows a comparison between the actual estimated frequency (9) (solid) and (14) (dashed) when a step variation of 1% is produced in the grid frequency, both normalized with respect to ω_o. In this simulation, the grid voltage is a pure sinusoid of amplitude 100 Vrms and nominal frequency $\omega_o = 2\pi 50$ rad/s, and the controller structure is described in Table II. As the figure shows, the setting time of (14) gives a reasonable criterion for choosing γ.

D. Implementation Issues

The addition of the frequency adaptation scheme to the current controller requires the online computation of the exponential functions of (2). This implies the online computation of trigonometric functions, which is usually performed through tables, increasing the memory requirements of the algorithm. To avoid the need of tables, we can take advantage of the fact that the estimated frequency (9) is actually allowed very small variations around ω_o (limited by the saturation). Therefore, the exponential functions can be very accurately approximated by their first-order Taylor series expansion around ω_o [16]. Hence

$$e^{hjT_s\hat{\omega}} \simeq e^{hjT_s\omega_o}\left(1 + hjT_s(\hat{\omega} - \omega_o)\right). \tag{17}$$

Note that this equation only requires product and add operations to be computed online and that $e^{hjT_s\omega_o}$ is a constant that can be computed offline. This allows the algorithm implementation in low-cost DSPs without significant additional memory requirements. The computation of these linearized exponentials requires a total of $1 + 2\xi$ add and 2ξ product operations to be implemented, where ξ is the total number of ROGIs in the implementation.

VI. Simulation Results

In this section, simulation results of the frequency-adaptive ROGI-based current controller are presented.

To test the capabilities of the frequency adaptation scheme, we will use the test voltage described in case 1 of Table I, plus an additional negative sequence fundamental component -1 (28.6%). The nominal frequency was set to $\omega_o = 2\pi 50$ rad/s, and the nominal fundamental component voltage was set to 100 Vrms. The controller structure was as described in Table II, and the frequency adaptation algorithm gain was $\gamma = 5 \times 10^5$ to achieve a setting time $t_{\text{set}} = 80$ ms, as described in Section V-C.

Fig. 8(a) shows the grid voltage. The signals shown are, from top to bottom, v_{sa}, v_{sb}, and v_{sc}. Fig. 8(b) shows the actual injected currents which are, from top to bottom, i_{sa}, i_{sb}, and i_{sc}. As can be seen, these signals are almost pure sinusoids in steady state. At $t = 0.4$ s, a step variation of $-1\%\omega_o$ is produced in the grid voltage frequency. As shown in Fig. 8(c), the estimated frequency (solid line) tracks this variation after a transient of 80 ms, as expected. This figure also shows the response of (14) to the same step frequency variation. As can be seen, the approximation is also valid when the grid is highly distorted. As a result of the estimated frequency ripple, the steady-state currents are slightly distorted, resulting in a THD $= 0.95\%$ for the most distorted phase. This THD can be further minimized by reducing γ, at the cost of a slower frequency estimation convergence speed. It is also worth noting that, during the frequency estimation transient, the currents become noticeably distorted, as shown in Fig. 8(b). This shows the importance of the frequency adaptation algorithm, without which the performance of the system would degrade in the presence of frequency variations.

VII. Experimental Results

In this section, the experimental results of the frequency-adaptive current controller are shown.

The controller was implemented in a fixed-point DSP TMS320F2812 with a clock frequency of 150 MHz using a sampling time $T_s = 100$ μs, and the pulse width modulation (PWM) update period of the VSC gate signals was set to $T_s/2$, which implies a delay $\tau = T_s/2$ in (1). The controller structure is described in Table II, and the frequency estimator gain was chosen as $\gamma = 5 \times 10^5$ to obtain $t_{\text{set}} = 80$ ms as in the previous section. The bus voltage was set to 550 V through a dc power source, and the applied phase voltage was 100 Vrms (supplied by a three-phase 380/100-Vrms Dy11 transformer connected to the 220-Vrms grid). The coupling inductance, which takes

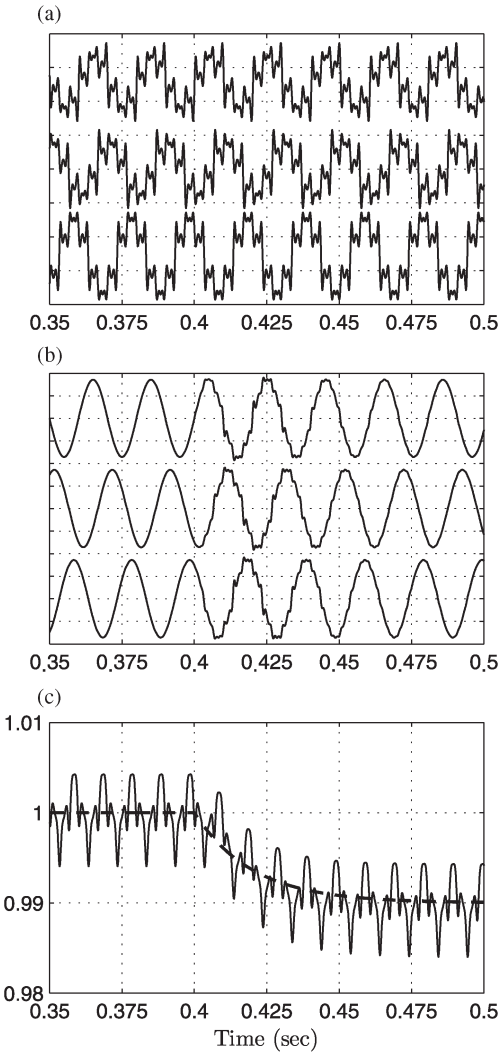

Fig. 8. Simulation results in the presence of a distorted voltage and a step frequency variation of $1\%\omega_o$. (a) Distorted grid voltage (175 V/div and THD $= 65.34\%$). (b) Actual current (5 A/div and THD $= 0.78\%$). (c) (Solid) Normalized estimated frequency $\hat{\omega}/\omega_o$ and (dashed) approximated dynamic response (14).

into account the leakage inductance of the transformer, was $L = 5.5$ mH.

Fig. 9(a) shows the applied three-phase voltage, which is 100 Vrms per phase, with a 50-Hz fundamental frequency and a THD $= 4\%$. In Fig. 9(b), the injected phase currents are shown for the controller with the frequency adaptation enabled. These currents are 7.5 Arms and have a THD $= 1.8\%$. Fig. 9(c) shows the phase currents again, but this time, the frequency adaptation is disabled and the estimated frequency is fixed at $\hat{\omega} = 1.01\omega_o$, with $\omega_o = 2\pi 50$ rad/s. As can be seen, these currents are noticeable distorted, even though the frequency was mistuned by approximately $1\%\omega_o$. In this case, the injected current THD was 3.17%, that is 57% higher than with the frequency adaptation enabled. This shows the importance of incorporating a frequency adaptation algorithm to the ROGI-based controller.

Since the grid frequency cannot be changed to observe the frequency estimator dynamic behavior, once $\hat{\omega}$ had converged to its steady-state value, at an arbitrary sample instant, the

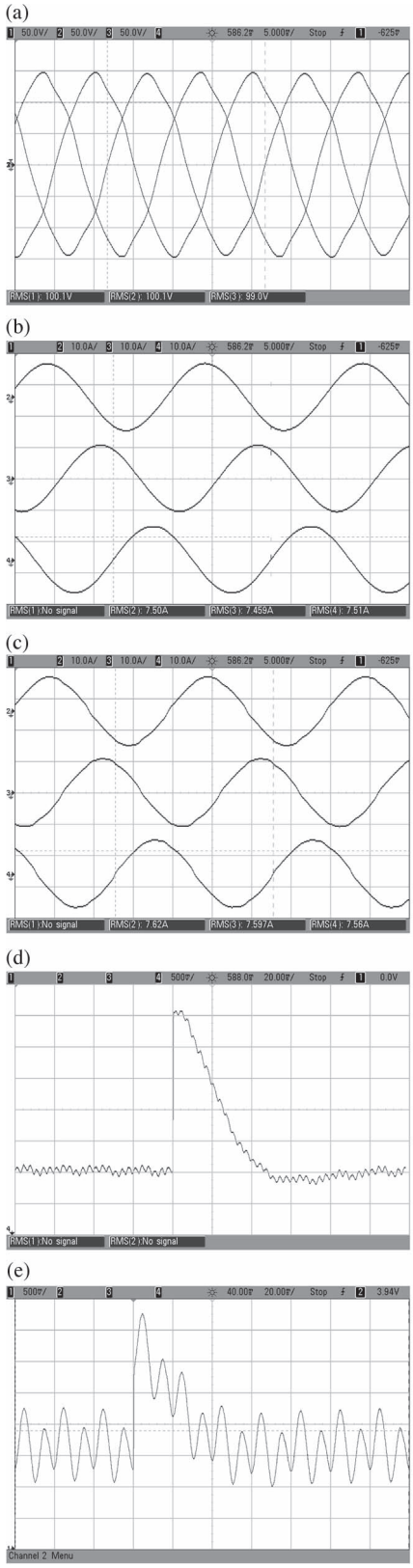

Fig. 9. Experimental results (horizontal: 5 ms/div). (a) Grid phase voltage (50 V/div and THD $= 4\%$). (b) Phase currents (10 A/div and THD $= 1.8\%$) with frequency adaptation enabled. (c) Phase currents (10 A/div and THD $= 3.17\%$) with estimated frequency fixed at $1.01\omega_o$. (d) Estimated frequency (horizontal: 20 ms/div; vertical: 0.1 Hz/div). (e) Estimated frequency, imbalance case (horizontal: 20 ms/div; vertical: 0.177 Hz/div). (a) Grid voltage. (b) Injected currents. (c) Injected currents ($\omega = 1.01\omega_o$). (d) $\hat{\omega}$. (e) $\hat{\omega}$ (imbalance).

estimated frequency was forced to be $\hat{\omega} = 1.01\omega_o$. This allows us to see the dynamic of the estimator as it converges again to the grid frequency. Fig. 9(d) shows the estimated frequency. This was measured through a PWM output of the DSP which was filtered through an RC filter with a cutoff frequency of 2340 Hz. As can be seen, the estimator converges around 80 ms, as predicted by the simulations.

Under severe voltage unbalanced conditions (SVUCs), the frequency estimator still converges. To show this, Fig. 9(e) shows the estimated frequency of the described controller performing the same test as in Fig. 9(d), but with one of the grid side voltages of the Dy11 transformer forced to neutral to produce imbalance. The figure shows that the estimated frequency behaves as expected for such SVUC, agreeing with the simulation results shown in Fig. 8(c) (where there was also imbalance). The injected currents and phase voltages behave as expected under SVUC [18] and are not included for space reasons.

The nonfrequency-adaptive ROGI-based current controller takes 7.99 μs to be computed. The inclusion of any frequency estimation algorithm requires an additional 2.05 μs to compute the linearized exponentials online through (17). The computation of the proposed frequency estimator (9) adds only 0.97 μs. This adds up to a total of 11.01 μs, keeping the controller as a very low computational burden proposal.

VIII. Conclusion

This paper has shown that a nonfrequency-adaptive ROGI-based current controller suffers a performance loss in the presence of grid frequency variations. To counter this effect, a simple frequency estimation law, which takes advantage of the controller's structure, is proposed. This law is given in a theoretical frame, and a method which allows its easy tuning is also presented. The resulting frequency-adaptive ROGI-based current controller allows to compensate grid voltage harmonics without performance lost in the presence of frequency variations and with very low computational burden. Both simulations and experimental results validate the proposal, being the last proof of the controller's implementation into a low-cost DSP.

Appendix I

In LQR theory, the feedback gains are chosen to minimize the cost function

$$J = \sum_{k=0}^{\infty} \vec{x}^H(k) Q \vec{x}(k) + R \left| \vec{u}_c^{\alpha\beta}(k) \right|^2$$

where $(.)^H$ denotes the transpose conjugate, $Q \in \mathbb{C}^{(2+N)\times(2+N)}$ is a Hermitian matrix, and $R \in \mathbb{R}$ are weighting factors. The solution is obtained by solving Riccati's algebraic equation [19]. In this paper, a diagonal weighting matrix Q is chosen, a simple choice commonly used in practice. With this choice, the diagonal elements of Q and R dictate how much each individual state and the input $\vec{u}_c^{\alpha\beta}$ contribute to the overall cost J. A method for choosing these weights is suggested in [22]. In this paper, the weights on Q and R (shown in Appendix II) were chosen giving priority to the following:

1) minimizing the energy in the injected current tracking error signal $(\vec{i}^{\alpha\beta} - \vec{i}_{\text{REF}}^{\alpha\beta})$;
2) avoiding excessive control efforts (which would saturate the PWM).

The energy of the tracking errors of the internal states of the controller were not prioritized. The first item was achieved by giving the first two states of the state vector $\vec{x}(k)$ a higher relative weight than the rest of the states. The second item was achieved by choosing R to limit the maximum control effort required in order to avoid actuator saturation under normal operating conditions (grid at nominal voltages, with low imbalance and THD $< 5\%$, with a dc bus voltage of 550 V). The actual values of Q and R were finally adjusted by trial and error.

Appendix II

The controller gains (K_h, K_p, and K_d in Fig. 2) are found using the LQR method with the parameters R and Q shown in Table II, where diag() represents a matrix whose main diagonal elements are those of the vector between square brackets.

TABLE I
Test Voltages (% of Fundamental Component)

	case 1 (THD=59.37%)	case 2 (THD=5%)
V_{-5}	34.1%	3.5%
V_7	27.3%	3.5%
V_{-11}	20.4%	1%
V_{13}	20.4%	0%
V_{-17}	10%	0%
V_{19}	5%	0%
V_{-23}	1%	0%
V_{25}	1%	0%

TABLE II
Simulation/Experimental System Setup

Symbol	Value	Reference
h	1, -1, -5, 7, -11, 13, -17, 19, -23, 25	ROGIs
T_s	100 μs	Sample time
τ	$T_s/2$	DSP delay
L	5.5 mH	Coupling ind.
g	0.07 A/V	Current gain
Q	diag([100 100 1 1 1 1 1 1 1 1 1 1])	LQR Q matrix
R	10	LQR R scalar

References

[1] T. Jin and J. Jimenez, "Review on planning and automation technologies for distributed generation systems," in *Proc. IEEE Conf. Autom. Sci. Eng.*, Aug. 2010, pp. 269–274.

[2] I. Balaguer, Q. Lei, S. Yang, U. Supatti, and F. Z. Peng, "Control for grid-connected and intentional islanding operations of distributed power generation," *IEEE Trans. Ind. Electron.*, vol. 58, no. 1, pp. 147–157, Jan. 2011.

[3] T. Zhou and B. Francois, "Energy management and power control of a hybrid active wind generator for distributed power generation and grid integration," *IEEE Trans. Ind. Electron.*, vol. 58, no. 1, pp. 95–104, Jan. 2011.

[4] A. Timbus, M. Liserre, R. Teodorescu, P. Rodriguez, and F. Blaabjerg, "Evaluation of current controllers for distributed power generation systems," *IEEE Trans. Power Electron.*, vol. 24, no. 3, pp. 654–664, Mar. 2009.

[5] Q. Zeng and L. Chang, "An advanced SVPWM-based predictive current controller for three-phase inverters in distributed generation systems," *IEEE Trans. Ind. Electron.*, vol. 55, no. 3, pp. 1235–1246, Mar. 2008.
[6] Q. Chunqing, Y. Yong, and S. Ji, "Deadbeat decoupling control of three-phase photovoltaic grid-connected inverters," in *Proc. Int. Conf. Mechatron. Autom.*, Sep. 2009, pp. 3843–3848.
[7] C.-M. Ho, V. Cheung, and H.-H. Chung, "Constant-frequency hysteresis current control of grid-connected VSI without bandwidth control," *IEEE Trans. Power Electron.*, vol. 24, no. 11, pp. 2484–2495, Nov. 2009.
[8] R. Gupta, "Generalized frequency domain formulation of the switching frequency for hysteresis current controlled VSI used for load compensation," *IEEE Trans. Power Electron.*, vol. 27, no. 5, pp. 2526–2535, May 2012.
[9] H. Mao, X. Yang, Z. Chen, and Z. Wang, "A hysteresis current controller for single-phase three-level voltage source inverters," *IEEE Trans. Power Electron.*, vol. 27, no. 7, pp. 3330–3339, Jul. 2012.
[10] M. Castilla, J. Miret, J. Matas, L. de Vicua, and J. Guerrero, "Linear current control scheme with series resonant harmonic compensator for single-phase grid-connected photovoltaic inverters," *IEEE Trans. Ind. Electron.*, vol. 55, no. 7, pp. 2724–2733, Jul. 2008.
[11] G. Shen, X. Zhu, J. Zhang, and D. Xu, "A new feedback method for PR current control of LCL-filter-based grid-connected inverter," *IEEE Trans. Ind. Electron.*, vol. 57, no. 6, pp. 2033–2041, Jun. 2010.
[12] Y. F. Wang and Y. W. Li, "Grid synchronization PLL based on cascaded delayed signal cancellation," *IEEE Trans. Power Electron.*, vol. 26, no. 7, pp. 1987–1997, Jul. 2011.
[13] F. Freijedo, A. Yepes, O. Löpez, A. Vidal, and J. Doval-Gandoy, "Three-phase PLLs with fast postfault retracking and steady-state rejection of voltage unbalance and harmonics by means of lead compensation," *IEEE Trans. Power Electron.*, vol. 26, no. 1, pp. 85–97, Jan. 2011.
[14] M. Mojiri, D. Yazdani, and A. Bakhshai, "Robust adaptive frequency estimation of three-phase power systems," *IEEE Trans. Instrum. Meas.*, vol. 57, no. 7, pp. 1793–1802, Jul. 2010.
[15] P. Rodriguez, A. Luna, I. Candela, R. Mujal, R. Teodorescu, and F. Blaabjerg, "Multiresonant frequency-locked loop for grid synchronization of power converters under distorted grid conditions," *IEEE Trans. Ind. Electron.*, vol. 58, no. 1, pp. 127–138, Jan. 2011.
[16] S. G. Jorge, C. Busada, and J. Solsona, "Frequency adaptive discrete filter for grid synchronization under distorted voltages," *IEEE Trans. Power Electron.*, vol. 27, no. 8, pp. 3584–3594, Aug. 2012.
[17] G. Xiaoqiang, W. Weiyang, and C. Zhe, "Multiple-complex coefficient-filter-based phase-locked loop and synchronization technique for three-phase grid-interfaced converters in distributed utility networks," *IEEE Trans. Ind. Electron.*, vol. 58, no. 4, pp. 1194–1204, Apr. 2011.
[18] C. A. Busada, S. Gomez-Jorge, A. E. Leon, and J. A. Solsona, "Current controller based on reduced order generalized integrators for distributed generation systems," *IEEE Trans. Ind. Electron.*, vol. 59, no. 7, pp. 2898–2909, Jul. 2012.
[19] R. J. Vaccaro, *Digital Control. A State-Space Approach*. New York: McGraw-Hill, 1995.
[20] W. Leonhard, *Control of Electrical Drives*, 2nd ed. Berlin, Germany: Springer-Verlag, 1996.
[21] K. Martin, "Complex signal processing is not complex," *IEEE Trans. Circuits Syst. I, Reg. Papers*, vol. 51, no. 9, pp. 1823–1836, Sep. 2004.
[22] A. E. Bryson and Y.-C. Ho, *Applied Optimal Control: Optimization, Estimation, and Control*. New York: Wiley, 1975.

Sebastián Gómez Jorge received the Electronics Engineer, M.S., and Dr. degrees from the Universidad Nacional del Sur, Bahía Blanca, Argentina, in 2006, 2009, and 2011, respectively.

He is currently with the Departamento de Ingeniería Eléctrica y de Computadoras, Instituto de Investigaciones en Ingeniería Eléctrica "Alfredo C. Desages," Universidad Nacional del Sur, where he is a graduate Teaching Assistant, and with CONICET, Buenos Aires, Argentina.

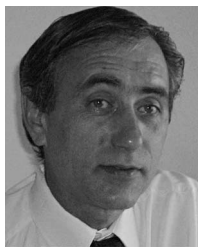

Claudio A. Busada was born in Bahía Blanca, Argentina, on March 13, 1962. He received the degree in electrical engineering and the Dr. degree in control systems from the Universidad Nacional del Sur (UNS), Bahía Blanca, in 1989 and 2004, respectively.

From 1988 to 2004, he was with the Mechanic and Electrical Department, City of Bahía Blanca. Since 1989, he has been with the Departamento de Ingeniería Eléctrica y de Computadoras, UNS, where he is a Professor. He is a Researcher of the the Instituto de Investigaciones en Ingeniería Eléctrica "Alfredo C. Desages" (UNS–CONICET). His research interests include power electronics, rotating machinery, active filters, automatic control, and integration of distributed energy systems.

Jorge A. Solsona (SM'04) received the Electronics Engineer and Dr. degrees from the Universidad Nacional de La Plata, La Plata, Argentina, in 1986 and 1995, respectively.

He is currently with the Departamento de Ingeniería Eléctrica y de Computadoras, Instituto de Investigaciones en Ingeniería Eléctrica "Alfredo C. Desages," Universidad Nacional del Sur, Bahía Blanca, Argentina, where he is a Professor, and with CONICET, Buenos Aires, Argentina. He is involved in teaching and research on control theory and its applications to electromechanical systems.